A&A, 677, A189 (2023)
https://doi.org/10.1051/0004-6361/202346386

Astronomy & Astrophysics

An advanced multipole model of the (130) Elektra quadruple system

M. Fuksa[1], M. Brož[1], J. Hanuš[1], M. Ferrais[2], P. Fatka[3], and P. Vernazza[2]

[1] Charles University, Faculty of Mathematics and Physics, Astronomical Institute, V Holešovičkách 2, 18000 Prague, Czech Republic
e-mail: fuksa@sirrah.troja.mff.cuni.cz
[2] Aix-Marseille Univ., CNRS, LAM, Laboratoire d'Astrophysique de Marseille, 13388 Marseille Cedex 13, France
[3] Astronomical Institute of the Czech Academy of Sciences, Fričova 298, Ondřejov 25165, Czech Republic

Received 11 March 2023 / Accepted 18 July 2023

ABSTRACT

Context. The Ch-type asteroid (130) Elektra is orbited by three moons, making it the first quadruple system in the main asteroid belt.
Aims. We aim to characterise the irregular shape of Elektra and construct a complete orbital model of its unique moon system.
Methods. We applied the All-Data Asteroid Modelling (ADAM) algorithm to 60 light curves of Elektra, including our new measurements, 46 adaptive-optics (AO) images obtained by the VLT/SPHERE and Keck/Nirc2 instruments, and two stellar occultation profiles. For the orbital model, we used an advanced N-body integrator, which includes a multipole expansion of the central body (with terms up to the order $\ell = 6$), mutual perturbations, internal tides, and the external tide of the Sun acting on the orbits. We fitted the astrometry measured with respect to the central body and also relatively, with respect to the moons themselves.
Results. We obtained a revised shape model of Elektra with the volume-equivalent diameter (201 ± 2) km. Of two possible pole solutions, $(\lambda, \beta) = (189; -88)$ deg is preferred, because the other one leads to an incorrect orbital evolution of the moons. We also identified the true orbital period of the third moon S/2014 (130) 2 as $P_2 = (1.642112 \pm 0.000400)$ days, which is in between the other periods, $P_1 \simeq 1.212$ days, $P_3 \simeq 5.300$ days, of S/2014 (130) 1 and S/2003 (130) 1, respectively. The resulting mass of Elektra, $(6.606^{+0.007}_{-0.013}) \times 10^{18}$ kg, is precisely constrained by all three orbits. Its bulk density is then (1.536 ± 0.038) g cm^{-3}. The expansion with the assumption of homogeneous interior leads to the oblateness $J_2 = -C_{20} \simeq 0.16$. However, the best-fit precession rates indicate a slightly higher value, ≃0.18. The number of nodal precession cycles over the observation time span 2014–2019 is 14, 7, and 0.5 for the inner, middle, and outer orbits.
Conclusions. Future astrometric or interferometric observations of Elektra's moons should constrain these precession rates even more precisely, allowing the identification of possible inhomogeneities in primitive asteroids.

Key words. minor planets, asteroids: individual: (130) Elektra – planets and satellites: fundamental parameters – astrometry – celestial mechanics – methods: numerical

1. Introduction

The asteroid (130) Elektra belongs to the primitive Ch spectral type objects (Rivkin et al. 2015). The visible and near-infrared spectral data for Ch- and Cgh-type asteroids most closely resemble those obtained for the unheated CM chondrite meteorites, and these asteroids therefore most likely represent their parent bodies (Vilas & Gaffey 1989; Vernazza et al. 2016). The only minor spectral variations among the largest Ch/Cgh bodies and the members of the associated collisional families are likely due to differences in the average grain size of the regolith particles. Therefore, CM parent bodies had homogeneous internal structures and did not experience significant (>300 °C) heating due to thermal evolution (Vernazza et al. 2016). Nevertheless, Elektra is not intact, because it experienced a collision, which is commonly the origin of small satellites (Durda et al. 2004; Benavidez et al. 2012).

Elektra is orbited by three satellites (also referred to as moons): S/2003 (130) 1 (Marchis et al. 2008), S/2014 (130) 1 (Yang et al. 2016), and S/2014 (130) 2 (Berdeu et al. 2022). The diameters of the moons as derived from their photometry are of the order of 6, 2, and 1.6 km. For the third moon, a short-periodic orbit was found, with a period of only 0.67 days (Berdeu et al. 2022).

Previous shape modelling of Elektra (Hanuš et al. 2017; Vernazza et al. 2021) indicates that the ecliptic latitude β is close to −88° or −89°. Hence, the ecliptic longitude λ remains poorly constrained, because even distant values of λ represent similar directions in space.

In this work, we revise the shape model together with the orbits of the moons. Most importantly, this helps us to resolve the ambiguity of poles, because the non-spherical shape of the central body induces a precession of the pericentres ω and nodes Ω, which is constrained by the astrometry of the moons. We also use additional photometric data, as described in Sect. 2.

From now on, bodies are denoted as follows: 0 – (130) Elektra, 1 – S/2014 (130) 1, 2 – S/2014 (130) 2, 3 – S/2003 (130) 1. As explained in Sect. 4, this order corresponds to the respective orbits: 1 – inner, 2 – middle, and 3 – outer. All physical and orbital quantities are numbered accordingly.

2. Data

2.1. Light curves, AO images, and stellar occultations of Elektra

For the shape reconstruction of Elektra, we prepared a data set consisting of 60 light curves, 46 AO images, and two

Table 1. Summary of optical disk-integrated light curves of (130) Elektra obtained in this work by the BlueEye600 robotic observatory.

N	Epoch	N_p	Δ (AU)	r (AU)	φ (°)	Filter
1	2022-03-01.2	112	2.66	3.62	4.3	R
2	2022-03-02.2	60	2.66	3.62	4.1	R
3	2022-03-03.2	39	2.65	3.62	3.9	R
4	2022-03-04.2	29	2.65	3.62	3.8	R
5	2022-03-10.2	71	2.66	3.63	3.5	R

Notes. Each line represents one light curve and contains the epoch, the number of individual measurements N_p, the asteroid's distances to the Earth Δ and the Sun r, phase angle φ, photometric filter and observation information.

stellar occultations. Most of the light curves (55 out of 60) were taken from the Database of Asteroid Models from Inversion Techniques (DAMIT[1]; Ďurech et al. 2010), which contains light curves and other input parameters in addition to shape models. The observational data covered the time span from 1980 to 2016. In March 2022, we expanded the set by measuring five new light curves (Table 1) using the BlueEye600 robotic observatory (Ďurech et al. 2018) located in Ondřejov. These light curves were obtained exclusively for this study and are now available in DAMIT together with the new shape and spin state solution. Moreover, we also uploaded them to the ACLDEF[2] database. All of the light curves used in this study, including the new measurements, can be found in Appendix D.

The set of AO images consists of two subsets. The first one from Hanuš et al. (2017) consists of 14 images captured by the Keck/Nirc2 instrument during the years 2002–2012 and two high-resolution infrared images were taken by the AO system VLT/SPHERE in 2014. The InfraRed Differential Imager and Spectrograph (IRDIS; Dohlen et al. 2008) and the Integral Field Spectrograph (IFS; Claudi et al. 2008) were used simultaneously to cover a more extended spectral range. The second subset of 30 images is taken from Vernazza et al. (2021). It was obtained by the Zurich IMaging POLarimeter (ZIMPOL; Schmid et al. 2018) during the summer of 2019. The two stellar occultations were taken from the Asteroidal Occultation Observers in Europe[3] database. The first event occurred on 21 April 2018 and was observed by 48 observers in total. After excluding 4 far misses and 6 chords with incorrect time indications, we were left with 38 usable chords. The second event occurred on 21 February 2021 and was observed by 17 observers. However, eight of the chords were non-detections. Although such chords are generally useful as 'strict' bounds for the asteroid's shape, we did not use them because the shape is already well constrained. Both occultation events are shown in Fig. 1.

2.2. Astrometric measurements of the moons

For the process of fitting the orbital parameters of the moons, it is crucial to have a sufficient set of positions, usually related to the central body or its photocentre. These positions were measured on the AO images of Elektra – with various methods – whenever some of its moons were visible.

[1] https://astro.troja.mff.cuni.cz/projects/damit/
[2] https://alcdef.org/
[3] http://www.euraster.net/index.html

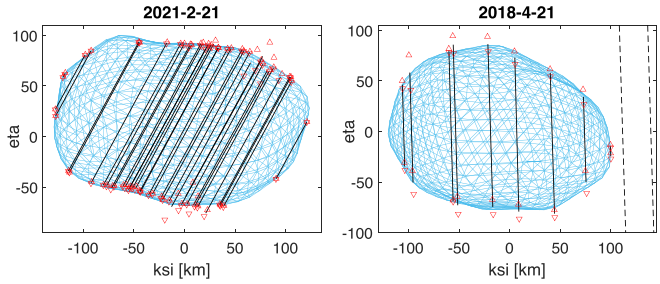

Fig. 1. Comparison of Elektra's shape model to chords from occultation events. The red triangles represent the timing uncertainties at the ends of each chord and the dashed lines are non-detection chords.

The first data set was taken from Berdeu et al. (2022), where the process of reduction, halo removal, and astrometry is explained in detail. Their data set is based on individual AO images of Elektra from December 2014 and consists of 120 positions of S/2014 (130) 1, 120 positions of S/2014 (130) 2, and 150 positions of S/2003 (130) 1. However, it is important to note that the individual positions are not mutually independent. Indeed, they correspond to a linear fit (in time) of 40 or 50 unique measurements. The second data set is based on 30 AO images from Vernazza et al. (2021). The images were reduced using the eclipse data reduction package (Devillard 1997). After reduction, the images were separately processed to remove the bright halo surrounding the asteroid, which was a necessary step to improve the detectability of the moons. To obtain the astrometric positions of the satellites, we used a specialised algorithm (Hanuš et al. 2013) that extracted the primary's contour and determined its photocentre. By fitting a Moffat-Gauss source profile to the moons and measuring from the photocentre, we obtained the 20, 20, and 12 new positions of the respective moons. Moreover, we computed the astrometric positions of the moons with respect to the other moons, which is handy to avoid any systematic related to the photocentre of the central body, or possibly centre-of-mass corrections.

The new positions are listed in Appendix B. Additionally, all astrometric data are available for download from the `Xitau`[4] webpage.

3. Shape reconstruction

3.1. All-Data Asteroid Modelling algorithm

The All-Data Asteroid Modelling (ADAM) algorithm (Viikinkoski et al. 2015) is a versatile inversion technique for the shape reconstruction of asteroids from various data types (AO images, light curves, occultations, radar, etc.). ADAM minimises the objective function, which is a measure of the difference between the Fourier-transformed image and the projected shape:

$$\chi^2 = w_{\mathrm{AO}} \sum_i \sum_{j=1}^{N_i} \left\| \mathcal{F}D_i(u_{ij}, v_{ij}) - \mathrm{e}^{2\pi i (o_i^x u_{ij} + o_i^y v_{ij}) + s_i} \mathcal{F}M_i(u_{ij}, v_{ij}) \right\|^2 + w_{\mathrm{LC}}\chi^2_{\mathrm{LC}} + w_{\mathrm{OC}}\chi^2_{\mathrm{OC}} + \sum_i w_i \gamma_i^2, \quad (1)$$

where $\mathcal{F}D_i(u_{ij}, v_{ij})$ is the Fourier transform of the data image D_i and $\mathcal{F}M_i(u_{ij}, v_{ij})$ is the Fourier transform of the projected

[4] https://sirrah.troja.mff.cuni.cz/~mira/xitau/

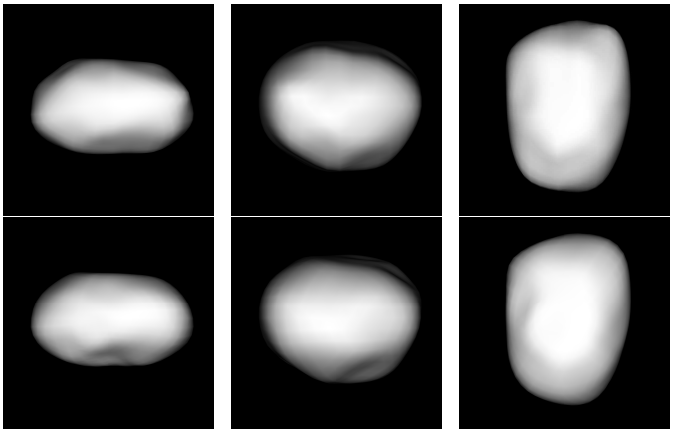

Fig. 2. Best-fit shape model (*top*) and the alternative shape model (*bottom*) from three different viewing geometries. The first two are equator-on views rotated by 90° and the third one is a pole-on view. The model is lit up artificially to highlight its finer surface details.

shape M_i, corresponding to the ith image and evaluated at the jth frequency point (u_{ij}, v_{ij}). The scale s_i and offset (o_i^x, o_i^y) are free parameters resolved during the optimisation. The additional term χ^2_{LC} is the standard square norm of the light-curve fit, while the term χ^2_{OC} is the model fit to stellar occultation chords. The implementation of the latter term in ADAM is described in Hanuš et al. (2017). The first three terms are multiplied by their corresponding weights w_{AO}, w_{LC}, and w_{OC} and the last term is a sum of regularisation functions γ_i multiplied by the weights w_i (Viikinkoski et al. 2015; Hanuš et al. 2017).

The data weights have an impact on the initial convergence of χ^2 and subjectively depend on the dataset; they are chosen to balance the individual χ^2 values and enable good convergence. Regularisation weights then help guide the convergence during the process.

Two shape representations are supported: octantoids and subdivisions. Octantoids are a global parametrisation, whereas subdivisions offer more local control. In this work, we used the octantoid shape representation. For a more detailed explanation, see Viikinkoski et al. (2015).

3.2. Best-fit and alternative shape models

We took a two-step approach. First, we aimed to get just a coarse shape model. Second, the shape resulting from the first optimisation was used as an initial model, and we then doubled the number of facets and the spherical harmonics degree in order to capture surface details. The initial conditions for the convergence, which are needed for the period and the pole, were taken from Vernazza et al. (2021).

Figure 2 and Table 2 present the best-fit and alternative shape models and their parameters. The best-fit model is a revised version of the shape model published in Vernazza et al. (2021), which is based on a larger dataset. Its pole coordinates were allowed to converge along with the shape to best fit the data. The alternative model is a shape model that converged with the pole fixed according to the coordinates inferred from our orbital model (Sect. 4).

The χ^2 map in Fig. 3 shows why the pole solution from ADAM remains unconstrained. Due to the close absolute distance of coordinates, there are many viable models. The best-fit model, denoted by a black tile, is in the upper left area of the map, while the alternative model is in a different local minimum

Table 2. Parameters of the best-fit (first line) and alternative (second line) models.

λ (deg)	β (deg)	P (h)	$a \times b \times c$ (km)	D_{eq} (km)
68.5	−88.9	5.224663	$267 \times 202 \times 151$	201.4 ± 1
188.2	−88.1	5.224664	$273 \times 230 \times 151$	202.3 ± 2

Notes. λ, β denote the ecliptic coordinates of the pole, P the period of rotation, a, b, c the extents along the main axes (The extents a, b, c were obtained using the overall dimensions technique (Torppa et al. 2008).), and D_{eq} denotes the diameter of the volume-equivalent sphere. The 1σ uncertainties on D_{eq} are based on the distribution from Fig. 4.

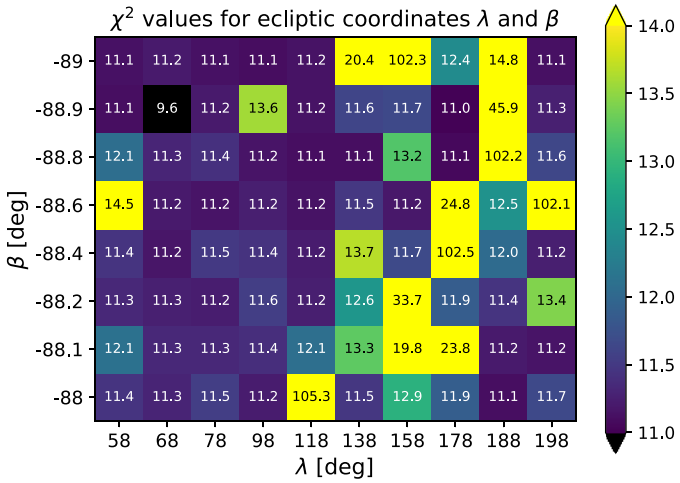

Fig. 3. χ^2 map for pole coordinates λ and β, where each value of χ^2 is represented by a colour from the colour bar. The black tiles indicate values below the range of the colour bar, while the yellow tiles indicate values above the range of the colour bar.

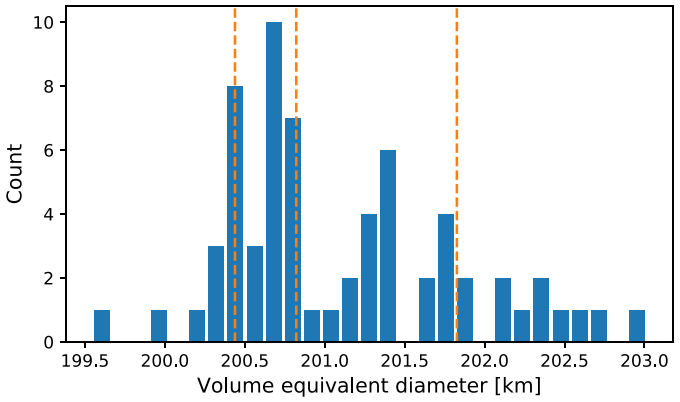

Fig. 4. Distribution of D_{eq} values based on shape models with χ^2 values below 12. The 16%, 50%, and 84% percentiles of the distribution are shown with orange lines.

in the bottom right area of the map. We propose that this alternative local minimum is where the true orbital pole lies. In Sect. 4, we even present a counterexample model based on the shape pole solution to support this.

We plotted a distribution of volume values from the dataset of models obtained from the χ^2 mapping (Fig. 4). By looking at the 16%, 50%, and 84% percentiles of the distribution we determined the uncertainties of D_{eq} in Table 2.

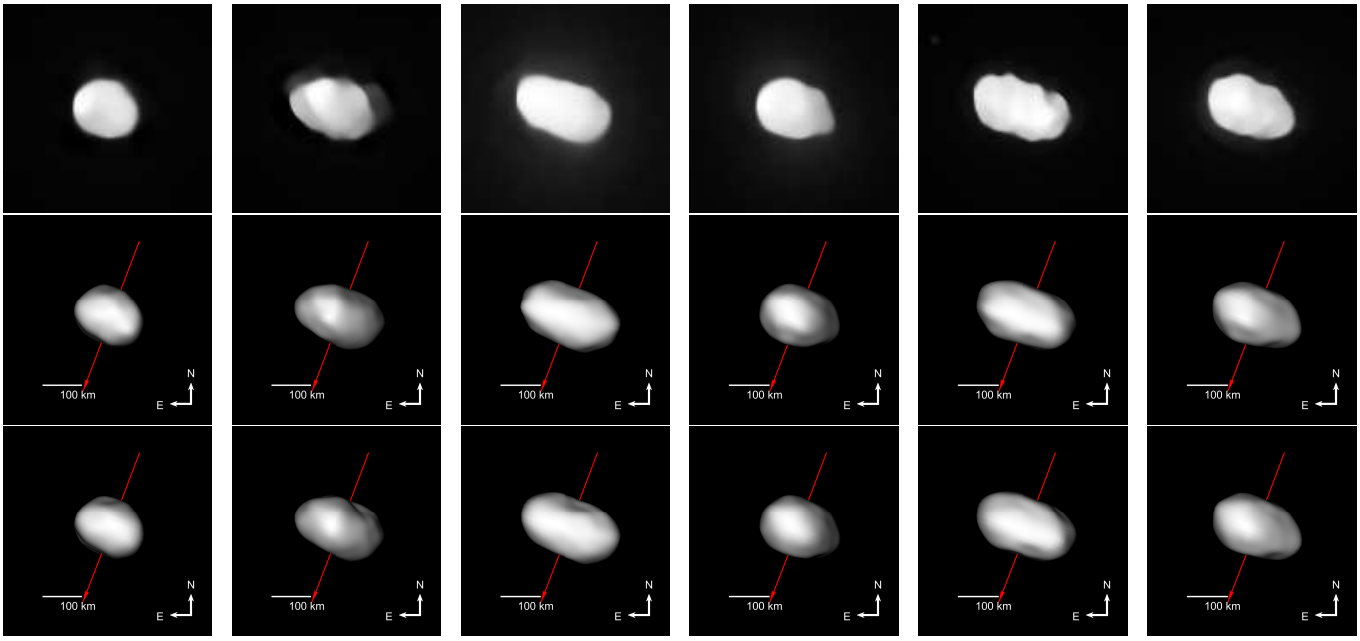

Fig. 5. AO images of Elektra (*top*), the best-fit shape model (*middle*), and the alternative shape model (*bottom*), all shown from the same viewing angle. The rotation axis is indicated by the red arrow.

The comparison of these two models with several AO images from the 2019 data set is given in Fig. 5. In the comparison and Fig. 2, we see that the overall shape of the alternative model is more rounded, with fewer surface features in some areas. However, this is in the range of expected differences dependent on regularisations. Both models are statistically and visually almost identical.

In the last two columns of Fig. 5, we see that the local topography present in the two AO images is not captured by either of the models. We tried using the subdivision shape representation and locally forcing those features, but it seems that they are not supported by the rest of the dataset, and forcing them just makes the overall fit worse.

For both models, we used the following weights: $w_{\rm LC} = 1.5$, $w_{\rm AO} = 0.85$, $w_{\rm OC} = 0.019$, and standard values for the regularisation weights. In Appendix D, we compare the best-fit model to all the observed light curves.

3.3. Multipole coefficients

Our orbital model has to be evolved over approximately 1000 days. On such a timescale, approximating the central body as a point mass is insufficient. Therefore, we computed a multipole expansion of the gravitational field up to the order of $\ell = 10$. The expansion is based on the Delaunay triangulation of the ADAM shape model made using the TetGen program (Si 2006). The respective definitions of the multipole coefficients are as follows:

$$C_{\ell 0} = \frac{1}{MR^\ell} \int_V \rho |\boldsymbol{r}|^\ell P_\ell(\cos\theta)\,\mathrm{d}V, \tag{2}$$

$$C_{\ell m} = \frac{2}{MR^\ell} \frac{(\ell-m)!}{(\ell+m)!} \int_V \rho |\boldsymbol{r}|^\ell P_{\ell m}(\cos\theta)\cos(m\phi)\,\mathrm{d}V, \tag{3}$$

$$S_{\ell m} = \frac{2}{MR^\ell} \frac{(\ell-m)!}{(\ell+m)!} \int_V \rho |\boldsymbol{r}|^\ell P_{\ell m}(\cos\theta)\sin(m\phi)\,\mathrm{d}V, \tag{4}$$

where r, θ, ϕ are the body-frozen spherical coordinates, M the mass of the body, R the reference radius of the gravitational model, P_ℓ, $P_{\ell m}$ the Legendre and associated Legendre polynomials, and $C_{\ell m}$, $S_{\ell m}$ are the respective coefficients.

Table 3 lists the results of Eqs. (2)–(4) evaluated for our best-fit shape model with homogeneous density. We found that an expansion up to the order $\ell = 2$ is sufficient to account for the precession of orbits and the higher orders (up to $\ell = 6$) were used to confirm that their contribution is in fact negligible.

Most notable is the oblateness coefficient $J_2 = -C_{20} \approx 0.159$. This is a relatively high value; only a few 100 km asteroids have a similar c/a axial ratio to that of (130) Elektra (Vernazza et al. 2021); for example (7) Iris, (16) Psyche, (22) Kalliope, and (45) Eugenia. The value inferred from shape will be compared to the dynamical oblateness in Sect. 4.6.

The alternative shape model has an almost equivalent $J_2 \simeq 0.162$. This corresponds to an uncertainty of only 0.003. We verified that the discretisation error of J_2 arising from the finite number of tetrahedrons is less than 0.001.

4. Orbital model

4.1. The dynamics included in the model

We use the N-body model called `Xitau`[5] based on the Bulirsch-Stoer integrator from Levison & Duncan (1994) that was substantially modified (Brož 2017; Brož et al. 2021, 2022a) to include the multipole expansion (up to the order $\ell = 10$), the tidal evolution, the external tides, and in particular, the fitting 'machinery'. To compare the model with the observations, we use the following unreduced metric[6]:

$$\chi^2 = \chi^2_{\rm sky} + \chi^2_{\rm sky2} + w_{\rm ao}\chi^2_{\rm ao}\,, \tag{5}$$

$$\chi^2_{\rm sky} = \sum_{j=1}^{N_{\rm bod}} \sum_{i=1}^{N_{\rm sky}} \left[\frac{(\Delta u_{ji})^2}{\sigma^2_{\text{sky major }ji}} + \frac{(\Delta v_{ji})^2}{\sigma^2_{\text{sky minor }ji}} \right], \tag{6}$$

[5] https://sirrah.troja.mff.cuni.cz/~mira/xitau/

[6] i.e. not divided by N; the number of measurements.

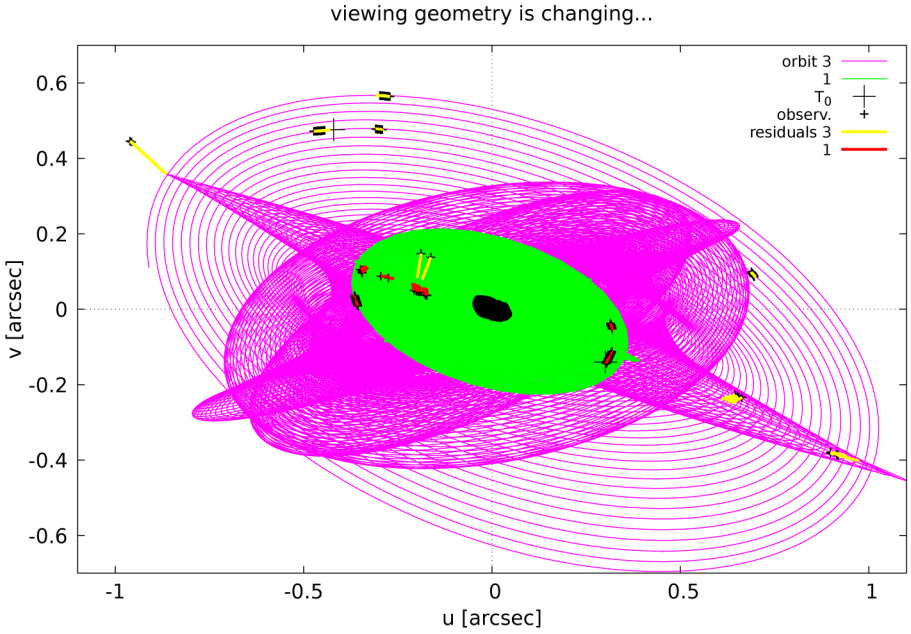

Fig. 6. Keplerian model of orbits 1 and 3 with $\chi^2 = 2195$ over the time-span of 1707 days. The orbits are plotted in the $(u; v)$ coordinates (green and pink lines, respectively), together with observed positions (black crosses), and residuals (red and yellow lines, respectively). Elektra's shape for one of the epochs is overplotted in black.

Table 3. Multipole coefficients (up to $\ell = 6$) of Elektra's gravitational field derived from the ADAM shape, assuming homogeneous density.

C_{00}	$+1.00000000$		
C_{10}	$+0.00000000$		
C_{11}	$+0.00000000$	S_{11}	$+0.00000000$
C_{20}	$-1.59109015 \times 10^{-1}$		
C_{21}	$-7.06376507 \times 10^{-5}$	S_{21}	$-1.73622001 \times 10^{-4}$
C_{22}	$-4.46764263 \times 10^{-2}$	S_{22}	$+5.16249277 \times 10^{-6}$
C_{30}	$+1.52377403 \times 10^{-3}$		
C_{31}	$-4.71344916 \times 10^{-4}$	S_{31}	$-2.13299430 \times 10^{-3}$
C_{32}	$+1.68475688 \times 10^{-3}$	S_{32}	$+7.99513867 \times 10^{-4}$
C_{33}	$-7.99140262 \times 10^{-4}$	S_{33}	$+1.61094232 \times 10^{-3}$
C_{40}	$+5.47386330 \times 10^{-2}$		
C_{41}	$+1.84595619 \times 10^{-3}$	S_{41}	$-1.98090953 \times 10^{-3}$
C_{42}	$+4.18945086 \times 10^{-3}$	S_{42}	$-1.56934242 \times 10^{-4}$
C_{43}	$+1.63489342 \times 10^{-4}$	S_{43}	$+8.16971619 \times 10^{-6}$
C_{44}	$+1.19047276 \times 10^{-4}$	S_{44}	$-1.04901431 \times 10^{-4}$
C_{50}	$-3.05649267 \times 10^{-3}$		
C_{51}	$+3.70902439 \times 10^{-4}$	S_{51}	$+1.27208068 \times 10^{-4}$
C_{52}	$-5.69391535 \times 10^{-4}$	S_{52}	$-2.33343309 \times 10^{-4}$
C_{53}	$+7.24854310 \times 10^{-5}$	S_{53}	$-1.50240727 \times 10^{-4}$
C_{54}	$-3.17247273 \times 10^{-5}$	S_{54}	$-1.43162546 \times 10^{-5}$
C_{55}	$+1.64621165 \times 10^{-5}$	S_{55}	$-1.89458984 \times 10^{-5}$
C_{60}	$-2.54715420 \times 10^{-2}$		
C_{61}	$-1.11217188 \times 10^{-3}$	S_{61}	$+1.69598512 \times 10^{-3}$
C_{62}	$-9.25476914 \times 10^{-4}$	S_{62}	$+6.44072903 \times 10^{-5}$
C_{63}	$-4.83382376 \times 10^{-5}$	S_{63}	$+1.27210479 \times 10^{-5}$
C_{64}	$-6.40791927 \times 10^{-6}$	S_{64}	$+6.56867385 \times 10^{-6}$
C_{65}	$-2.07536310 \times 10^{-6}$	S_{65}	$-7.77372686 \times 10^{-7}$
C_{66}	$+6.05696810 \times 10^{-7}$	S_{66}	$+5.52013261 \times 10^{-7}$

$$\chi^2_{\mathrm{sky2}} = \sum_{i=1}^{N_{\mathrm{sky2}}} \left[\frac{(\Delta u_i)^2}{\sigma^2_{\mathrm{sky\ major}\,i}} + \frac{(\Delta v_i)^2}{\sigma^2_{\mathrm{sky\ minor}\,i}} \right], \tag{7}$$

$$\chi^2_{\mathrm{ao}} = \sum_{i=1}^{N_{\mathrm{ao}}} \sum_{k=1}^{360} \frac{(u'_{ik} - u_{ik})^2 (v'_{ik} - v_{ik})^2}{\sigma^2_{\mathrm{ao}\,i}}, \tag{8}$$

where the index i corresponds to the observational data, j to individual bodies, k to angular steps of silhouette data, $'$ to synthetic data interpolated to the times of observations, u, v are the sky-plane coordinates, and σ the observational uncertainties along the two axes (denoted 'major' and 'minor' for ellipsoidal uncertainties).

The 'goodness-of-fit' terms χ^2_{sky} and χ^2_{sky2} correspond to the absolute astrometry (i.e. with respect to body 0) and the relative astrometry (e.g. body 2 with respect to body 1). Optionally, we also include the regularisation term χ^2_{ao} derived from silhouettes (as explained in Brož et al. 2021), which prevents pole orientations incompatible with the shape. This term is multiplied by the weight w_{ao}, which has no relation to the weight term w_{ao} from Eq. (1).

Using both χ^2_{sky} and χ^2_{sky2} is useful because they are not exactly the same measurements. Computing the relative positions removes any systematics related to the photocentre and provides more precise (relative) information. We note that this rapidly increases the overall number of measurements, as each AO image where two or three moons are visible at the same time is counted again for each relative measurement taken.

In the following, we present two orbital models of increasing complexity. In both of them, we account for the external tide exerted by the Sun. The necessary ephemerides were obtained from the Jet Propulsion Laboratory (JPL; Park et al. 2021).

4.2. Keplerian model

Initially, by manual fitting and then by converging with the simplex algorithm (Nelder & Mead 1965), we constructed a simplified Keplerian model for the already well-known moons: S/2014 (130) and S/2003 (130), that is, a model of orbits 1 and 3. The masses of the moons were neglected and the central body was taken as a point of mass. These preliminary orbits are shown in Fig. 6.

In the case of the Elektra system, a Keplerian model is accurate enough for a time span of about a month, as can be seen in Berdeu et al. (2022), but is insufficient for the time span of 1707 days. The resulting value of $\chi^2 = 2195$ is too high compared to the number of measurements (i.e. 430). The residuals in

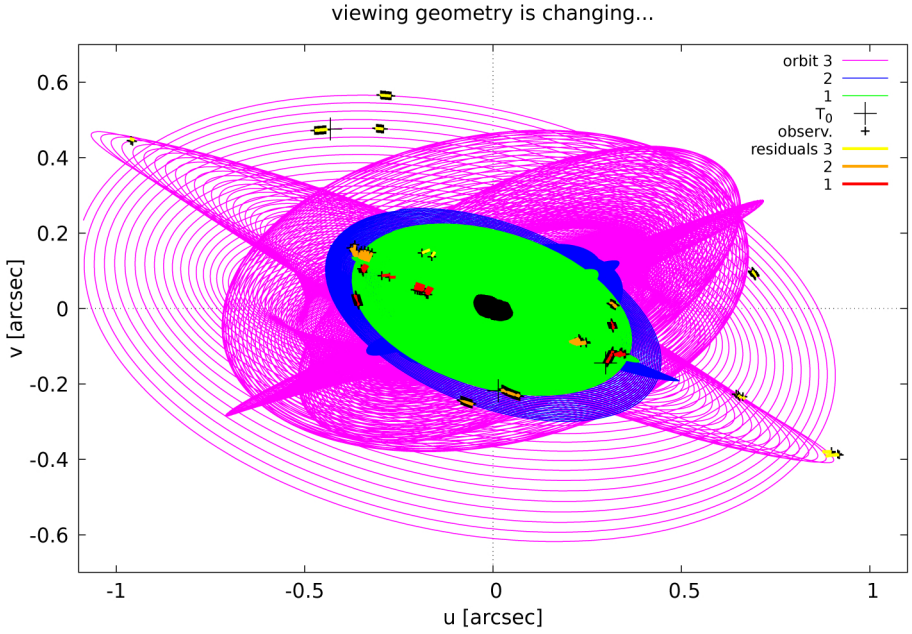

Fig. 7. Quadrupole model of the orbits 1, 2, and 3 with $\chi^2 = 1084$ over the time-span of 1707 days. The orbits are plotted in the $(u; v)$ coordinates (green, blue and pink lines, respectively), together with observed positions (black crosses) and residuals (red, orange and yellow lines, respectively). Elektra's shape for one of the epochs is overplotted in black.

Fig. 6 exhibit large systematic uncertainties. In the top left part in particular, the synthetic orbit is far from that suggested by observations. This is due to the missing nodal precession, which must be present given the non-negligible oblateness ($J_2 = -C_{20}$) of the central body.

4.3. Best-fit quadrupole model

We present a quadrupole model of the full system in Figs. 7 and 8. In this more complex model, the masses of the moons are taken into account and the gravitational field of the central body was expanded up to the order $\ell = 2$ (according to Table 3), assuming homogeneous density. When evaluated with the full metric (Eq. (5)) with the weight $w_{ao} = 0.3$, the model is a best-fit one with $\chi^2 = 1084$.

This model is the result of a long series of models, which were being improved with every iteration. It was much more efficient to only use up to $\ell = 2$, which is sufficient for a satisfying model.

We list the parameters of this best-fit model in Tables 4 and 5. They are given as osculating for the epoch $T_0 = 2457021.567880$ (TDB), but these elements are not constant. Due to the oblateness of Elektra and its massive moons, the orbital elements oscillate over time, as can be seen in Figs. 9–11. The peak-to-peak amplitudes of some of these elements are substantial, and so it is not surprising that the Keplerian model is insufficient. From the circulation of the arguments of pericentre, we determined the apsidal precession of the moons: $\dot{\omega}_1 = 5.9\,\mathrm{deg\,day^{-1}}$, $\dot{\omega}_2 = 2.9\,\mathrm{deg\,day^{-1}}$, and $\dot{\omega}_3 = 0.19\,\mathrm{deg\,day^{-1}}$.

The uniqueness of our solution lies in the precession cycles of Ω and ϖ (Figs. 9–11). The two innermost orbits have many cycles; that is, about 14 cycles of Ω_1 and ϖ_1 and about 7 cycles of Ω_2 and ϖ_2. A correct orbital solution could be one with two and one cycle less, respectively. Thankfully, we also have the outer moon and its orbit with only a half cycle of Ω_3 and ϖ_3, which cannot be made one cycle more or less without being a completely different and unviable solution. Therefore, even the number of precession cycles of the two innermost moons is well constrained because the central body is the same.

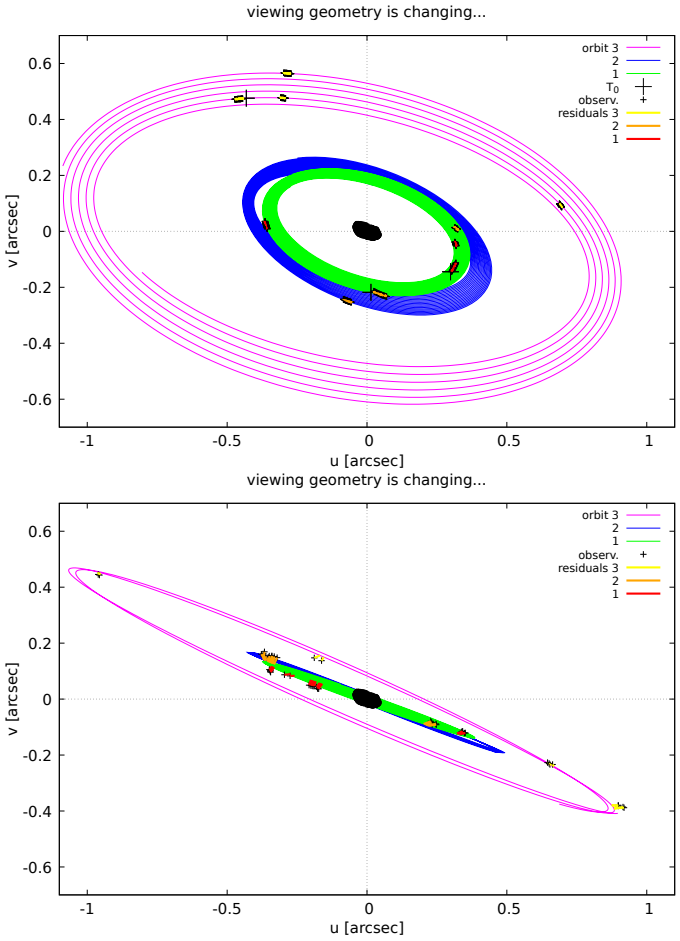

Fig. 8. Same as Fig. 7, but plotted separately for each data set: Berdeu et al. (2022, *top*) and Vernazza et al. (2021, *bottom*).

Having the precise mass of Elektra, $(6.606^{+0.007}_{-0.013}) \times 10^{18}$ kg, we can combine it with the volume of the shape model, $(4.3 \pm 0.1) \times 10^6$ km^3, and obtain the precise bulk density, $\bar{\rho} = (1.536 \pm 0.038)$ g cm^{-3}. Since we use multipole expansion, our orbital

Table 4. Parameters of the best-fit model, given with uncertainties.

		Best-fit model	Counter-example model
$\chi^2_{\rm sky} + \chi^2_{\rm sky2}$		872	19903
$N_{\rm measurements}$		837	837
Variable	Unit	Value with uncertainty	Value
$\lambda_{\rm pole}$	deg	188.3 ± 2.6	68.5
$\beta_{\rm pole}$	deg	-88.2 ± 0.2	-88.9
$M_{\rm total}$	M_S	$(3.322^{+0.003}_{-0.006}) \times 10^{-12}$	3.323×10^{-12}
q_1	1	$(1.02 \pm 0.55) \times 10^{-6}$	0.97×10^{-6}
q_2	1	$(5.2 \pm 5.4) \times 10^{-7}$	2.7×10^{-7}
q_3	1	$(2.74 \pm 0.12) \times 10^{-5}$	5×10^{-5}
P_1	day	1.2127 ± 0.0002	1.2127
e_1	1	0.028 ± 0.005	0.068
i_1	deg	179.7 ± 0.6	191.9
Ω_1	deg	275.3 ± 11.9	265.2
ϖ_1	deg	324.3 ± 18.5	25.8
λ_1	deg	343.2 ± 24.1	347.9
P_2	day	1.6421 ± 0.0004	1.6420
e_2	1	0.064 ± 0.007	0.060
i_2	deg	183.7 ± 0.3	184.1
Ω_2	deg	197.1 ± 7.5	194.7
ϖ_2	deg	107.9 ± 12.1	65.5
λ_2	deg	248.5 ± 15.2	244.9
P_3	day	5.30032 ± 0.00015	5.30041
e_3	1	$0.123^{+0.004}_{-0.002}$	0.156
i_3	deg	175.3 ± 0.2	173.8
Ω_3	deg	133.5 ± 2.1	129.7
ϖ_3	deg	$356.8^{+4.3}_{-1.3}$	6.6
λ_3	deg	$291.1^{+4.3}_{-0.1}$	289.1

Notes. Also, for completeness, we provide the parameters of a counter-example model based on the rotational pole given by the ADAM algorithm in Sect. 3. The listed χ^2 is with the weight $w_{\rm ao}$ set to zero and $N_{\rm measurements}$ is the number of all astrometry measurements, both absolute and relative. Orbital elements are referred to the epoch $T_0 = 2457021.567880$ (TDB). Uncertainties are given at 1σ. $\lambda_{\rm pole}$ and $\beta_{\rm pole}$ are the ecliptic longitude and latitude of Elektra's rotational pole. $M_{\rm total}$ is the total mass of the system, $q_1 = m_1/m_0$, $q_2 = m_2/(m_0 + m_1)$, and $q_3 = m_3/(m_0 + m_1 + m_2)$ are the mass ratios, where m_0 denotes the mass of the central body (i.e. Elektra), m_1 the mass of body 1 (inner moon S/2014 1), m_2 the mass of body 2 (middle moon S/2014 2), m_3 the mass of body 3 (outer moon S/2003), P_k the orbital period of the corresponding orbit, e_k eccentricity, i_k inclination, Ω_k the longitude of the nodes, ϖ_k the longitude of the pericentre, and λ_k is the true longitude; $k = 1, 2, 3$.

Table 5. Dependent parameters of the best-fit model, given with uncertainties.

Variable	Unit	Value with uncertainty
m_0	M_S	$(3.322^{+0.003}_{-0.006}) \times 10^{-12}$
m_1	M_S	$(3.4 \pm 1.8) \times 10^{-18}$
m_2	M_S	$(1.7 \pm 1.8) \times 10^{-18}$
m_3	M_S	$(9.1 \pm 0.4) \times 10^{-17}$
a_1	km	496.8 ± 0.4
a_2	km	608 ± 0.5
a_3	km	1328 ± 0.9

Notes. m are the masses of the individual bodies and a are the semi-major axes. The same notation as in Table 4 is used.

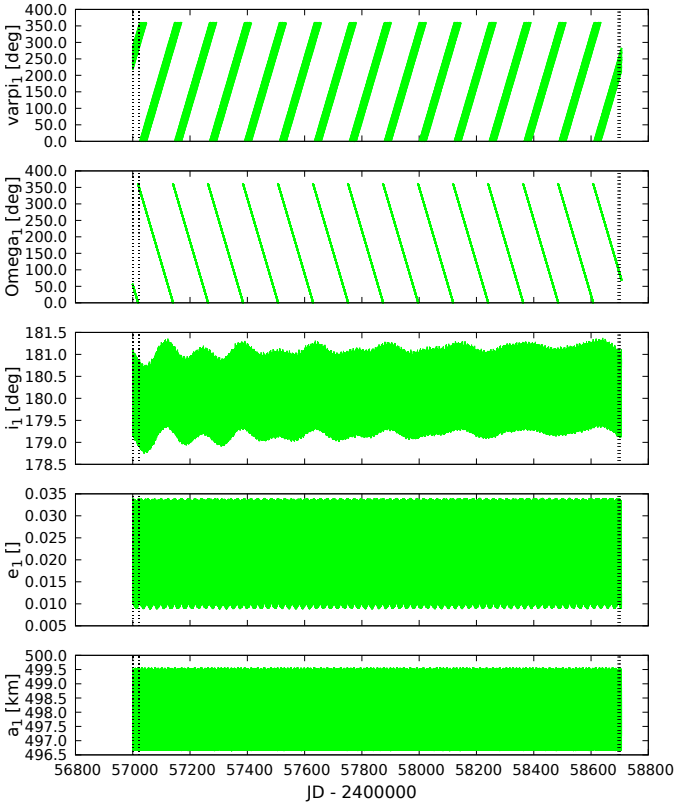

Fig. 9. Evolution of the osculating elements of the inner moon S/2014 1 plotted over the time span of 1707 days. Shown is the semimajor axis a_1, eccentricity e_1, inclination i_1, the longitude of the ascending node Ω_1, and the longitude of the periapsis ϖ_1.

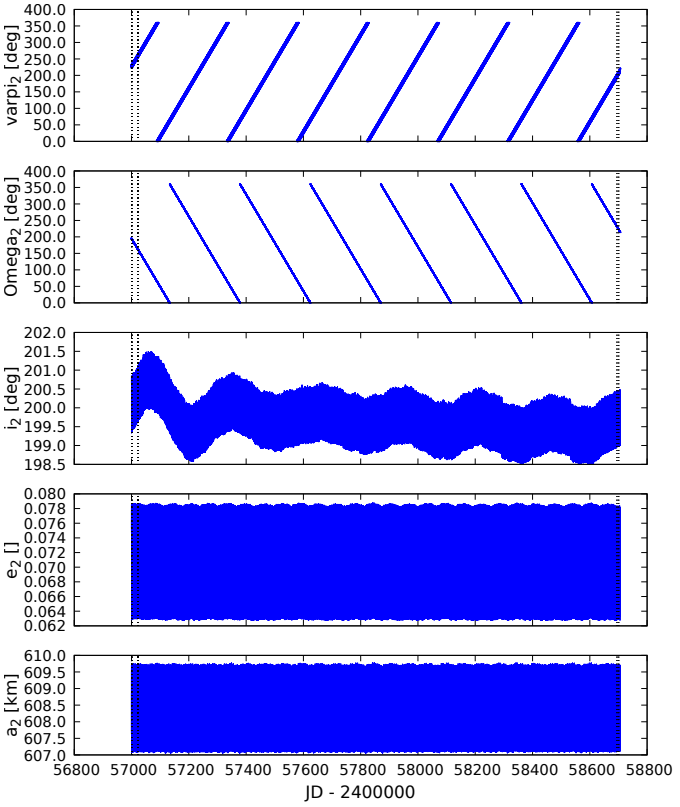

Fig. 10. Same as Fig. 9, but for the middle moon S/2014 2.

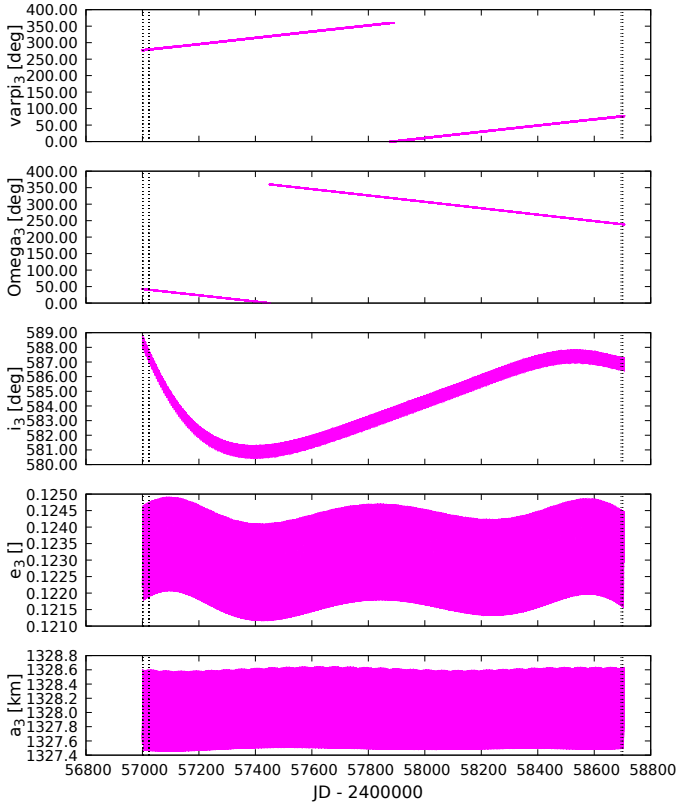

Fig. 11. Same as Fig. 9, but for the outer moon S/2003.

model sensitively depends on the orientation of the central body. Even a small change in the coordinates of the pole can completely change the satellite's orbits. Indeed, we obtained more precise pole coordinates, $\lambda_{\rm pole} = (188.3 \pm 2.6)$ deg and $\beta_{\rm pole} = (-88.2 \pm 0.2)$ deg, from our orbital model than from the shape model alone. Consequently, we derived an alternative shape model, as discussed in Sect. 3.

To demonstrate that these more precise pole coordinates are indeed preferable, we present a counterexample model in Table 4. This model is based on a rotational pole given by the ADAM algorithm in Sect. 3 and has a much higher χ^2 value, making it unviable.

4.4. MCMC analysis

The Markov chain Monte Carlo (MCMC; Robert & Casella 2011; Tierney 1994) is a method for randomly sampling probability distributions. To sample the distribution functions of the parameters of our orbital model we used the Python package emcee (Foreman-Mackey et al. 2013), which is an implementation of the MCMC.

We let all parameters of the model be free, including the rotational pole of Elektra, the total mass of the system, the mass ratios of the moons q_1, q_2, and q_3, and 18 orbital parameters, six for each orbit of the three moons. To initialise the chains, we started with the parameters of the best-fit model and set some a priori limits to keep the walkers around the local minimum of our preferred solution. The limits were an order of magnitude higher and lower for q_1, q_2 and q_3 to test if they are constrained, and a range of a few hours for the orbital periods. For other variables, the limits are relevant only in the case of Ω_1 and λ_1, because some part of their distribution lies beyond their upper limits, as can be seen in Fig. A.1. However, this should not notably affect the results.

We ran the MCMC with 48 walkers (i.e. two times 24; the number of free parameters) for 4000 iterations. However, as our limits on orbital periods were not narrow enough, about 15 walkers ended up migrating into neighbouring local minima, and so without the loss of generality, we removed them. We set the burn-in phase as 2000 iterations; after that, almost all parameters were in a steady state (Fig. A.2), except for q_1, q_2, $\log e_2$, and Ω_2 (and therefore ϖ_2 and λ_2), which still have some overall upward or downward trends. Regardless, this again should not notably affect the results.

From the MCMC, we obtained the uncertainties on the parameters. These are given in Table 4 at 1σ, also known as the 16% and 84% percentiles. In particular, we have a very precise determination of the total mass, because it was constrained by all three orbits.

The complete corner plot is shown in Fig. A.1. Some of the parameters are correlated with each other. First, we have a strong positive triple correlation in each set of Ω_i, ϖ_i, and λ_i, where $i = 1, 2, 3$. This is not surprising given the definitions of these parameters. The third triplet also has a positive correlation with $\log e_3$. This could be explained by the specific observation geometry during the respective epochs. The $\log e_3$ also has a negative correlation with i_3, which could also be due to the different observation geometries. Lastly, the first triplet has a positive correlation with the mass ratio q_3.

4.5. The third moon, S/2014 (130) 2

The Kepler solution presented by Berdeu et al. (2022) is a short-period (0.67 day) orbit of the third moon S/2014 (130) 2. However, it appears to 'cross' the orbit of the inner moon S/2014 (130) 1. Here, we present a 4-body model, which includes mutual interactions, multipoles ($\ell = 2$), and external tides. We surveyed all possible periods and tested both inner and outer orbits. In particular, we were interested in a co-orbital solution because the astrometric positions of S/2014 (130) 2 are always close to the orbit of S/2014 (130) 1.

The periodogram for the third moon is presented in Fig. 12. Its orbit is unstable below 0.58 day; 0.67 day is only one local minimum, but undeniably not the deepest. The co-orbital solutions have periods between 1.19 and 1.20 days, but none of them are deep enough, unfortunately. A regular series of minima is seen for longer periods, with 1.64 days being the deepest minimum.

This minimum is our preferred solution for S/2014 (130) 2. It is a stable orbit, close to the mean-motion resonance with S/2014 (130) 1. The ratio of periods 1.35 is not exactly 4/3, because of the respective critical angle:

$$\sigma = 4\lambda_2 - 3\lambda_1 + \varpi_1, \tag{9}$$

or alternatively:

$$\sigma' = 4\lambda_2 - 3\lambda_1 + \varpi_2 \tag{10}$$

includes a non-negligible precession contribution. Nevertheless, neither of these angles librates; a necessary period for an exact resonance is slightly shorter, $P_2 = 1.608$ days. Nonetheless, the proximity to the mean-motion resonance might be an independent indication of a correct solution (such as for (216) Kleopatra; Brož et al. 2021).

We also verified the influence of moon masses on their orbital evolution. According to our tests with mass ratios up to

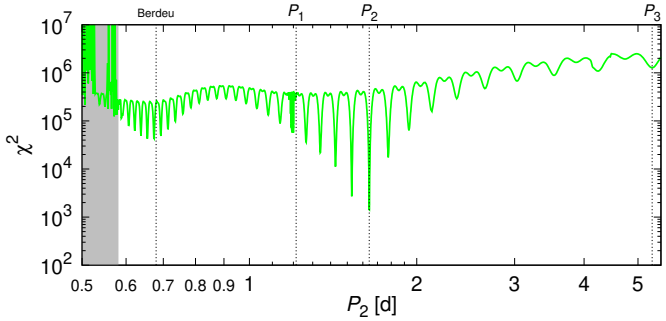

Fig. 12. Periodogram for the orbit of the third moon (S/2014 (130) 2). The χ^2 values were computed from the 2014 astrometric data only, without contributions for other moons. The osculating period P_2 was varied, while other elements were kept fixed. At the epoch T_0 = 2457021.567880 (TDB), the synthetic position was very close to the observed one. The best-fit period is 1.642 days. For comparison, the period of 0.678 days from Berdeu et al. (2022) is indicated.

10^{-4}, mutual perturbations are weak compared to the remaining systematic uncertainties in astrometry. Therefore, the moon masses remain unconstrained and the mass ratios inferred from photometry (approximately 10^{-6}, 5×10^{-7}, 3×10^{-5}) should be preferred.

4.6. Dynamical constraints for the oblateness

Having all three orbits, we performed a fitting of the oblateness C_{20} of the central body. We were interested not only in the best-fit model but also in poor fits, which enable us to reject the respective models. We computed an extended grid of models, with the oblateness C_{20} and the time lag Δt parameters kept fixed, while all other parameters were set free.

We included all multipole terms up to the order $\ell = 6$ (from Table 3) in order to ensure that none of these high-order contributions to the total precession rate is missed. We also verified that orders $\ell > 6$ only negligibly affect the value of χ^2. Initial conditions for the simplex algorithm (Nelder & Mead 1965) must be set up precisely; in particular, P_1, P_2, and P_3 must be close to the true or global minimum (for a given value of C_{20}), otherwise the simplex could be 'stuck'. We used two fully converged models for two different values of C_{20}; we verified these minima are global by a χ^2 mapping, knowing the typical spacing between the local minima, such as $\Delta P = P_1^2/(22.1\,\mathrm{days}) \doteq 0.066$ days, or $\Delta P' = P_1^2/(1701\,\mathrm{days}) \doteq 0.00086$ days, depending on the time span (2014 only, 2014–2019). Eventually, we determined the linear relations $P_1(C_{20})$, $P_2(C_{20})$, and $P_3(C_{20})$, and interpolated the periods accordingly.

Overall, the best-fit model has $\chi^2 = 932$, with contributions $\chi^2_{\mathrm{sky}} = 479$, $\chi^2_{\mathrm{sky2}} = 211$, and $\chi^2_{\mathrm{ao}} = 792$, where we used the weight $w_{\mathrm{ao}} = 0.3$. All models are summarised in Fig. 13. The best-fit value of $C_{20} \simeq -0.18$, with an uncertainty of less than 0.01. This is slightly larger than the value computed for a homogeneous body.

Most importantly, we did not find any fits with $C_{20} \simeq -0.16$ that have lower or comparable χ^2. On the contrary, the values were always significantly higher. This might be an indication of irregular, or (partially) differentiated internal structure; however, the irregularity should be more oblate, not more spherical.

Possible Elektra family. The nature of the meteorite analogue material (CM chondrites) and its average density ($2.13\,\mathrm{g\,cm^{-3}}$) imply a substantial porosity of 28% for Elektra.

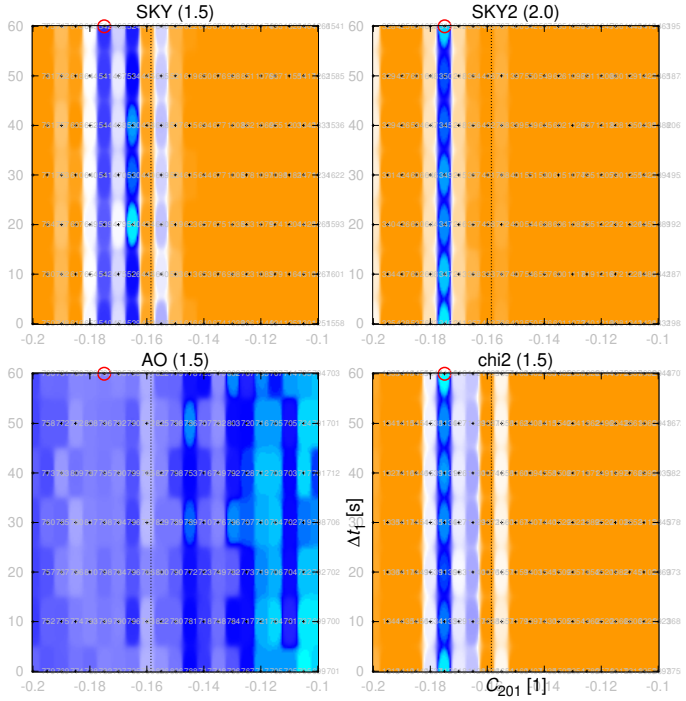

Fig. 13. Overview of best-fit models of the (130) system for the pair of fixed parameters: oblateness $C_{20,1}$ and tidal time lag Δt_1 (Brož et al. 2022a) of the central body. All other parameters were free. Each of the 147 models was converged for up to 1000 iterations, that is 147 000 models in total. The χ^2 values are plotted as colours: cyan corresponds to the overall best fit, blue to good fits (1.2 times the best fit), orange to poor fits (1.5). The four panels correspond to the χ^2 contributions: astrometry (SKY), relative astrometry of the moons (SKY2), silhouettes of the central body (AO), and the weighted sum of them.

If these findings are accurate, a re-accumulation event might be at the origin of Elektra itself (and its satellite system). Usually, the event ends with a re-accumulation of streams (see e.g. Brož et al. 2022b), which deposit loose, low-dense, rubble-pile material, creating 'hills', some of which could be observed at the limb (see e.g. Fig. 5, top row, fifth column). Fragments from this event should also form a family. Even though there is no 'official' Elektra family (Nesvorný et al. 2015), (130) Elektra is embedded in the Alauda family ((702), FIN 902[7]). Given all of the arguments above, a part of this family should belong to Elektra; in particular, bodies with lower semimajor axis ($a < 3.07$ au), which do have similar inclinations to (130) Elektra ($\sin i \simeq 0.38$).

5. Conclusions

We present the first self-consistent model for all three moons of (130) Elektra. The model covers a considerably long time span (2014–2019) requiring a sufficiently complex dynamical model, including at least oblateness ($\ell = 2$), which induces precession. With the constraint of three orbits and assuming a homogeneous internal structure, we obtain a precise mass for Elektra of $(6.606^{+0.007}_{-0.013}) \times 10^{18}$ kg.

The relative astrometry of the moons seems more reliable than measurements with respect to (130) Elektra, because any possible issues with determining the photocentre of the primary are absent. The relative astrometry strongly suggests a dynamical oblateness of $J_2 \simeq 0.18$, even with the high-order ($\ell = 6$)

[7] Family Identification Number = 902 (Nesvorný et al. 2015).

multipoles included, which also contribute to the total precession. This higher oblateness would either require some internal structure or a substantial modification of the shape, 'enforced' by the observed precession. In the future, this should lead to new 'photo-dynamical' shape reconstruction methods.

Acknowledgements. The Czech Science Foundation supported this work through grants GA22-17783S (M.F., J.H.) and GA21-11058S (M.B.). In this work, measurements from the BlueEye600 telescope, supported by Charles University, were used.

References

Benavidez, P. G., Durda, D. D., Enke, B. L., et al. 2012, Icarus, 219, 57
Berdeu, A., Langlois, M., & Vachier, F. 2022, A&A, 658, A4
Brož, M. 2017, ApJS, 230, 19
Brož, M., Marchis, F., Jorda, L., et al. 2021, A&A, 653, A56
Brož, M., Ďurech, J., Carry, B., et al. 2022a, A&A, 657, A76
Brož, M., Ferrais, M., Vernazza, P., Ševeček, P., & Jutzi, M. 2022b, A&A, 664, A69
Claudi, R. U., Turatto, M., Gratton, R. G., et al. 2008, in Ground-based and Airborne Instrumentation for Astronomy II, 7014, 1188
Devillard, N. 1997, The Messenger, 87, 19
Dohlen, K., Langlois, M., Saisse, M., et al. 2008, in Ground-based and Airborne Instrumentation for Astronomy II, 7014, 1266
Durda, D. D., Bottke, W. F., Enke, B. L., et al. 2004, Icarus, 170, 243
Ďurech, J., Sidorin, V., & Kaasalainen, M. 2010, A&A, 513, A46
Ďurech, J., Hanuš, J., Brož, M., et al. 2018, Icarus, 304, 101
Foreman-Mackey, D., Hogg, D. W., Lang, D., & Goodman, J. 2013, PASP, 125, 306
Hanuš, J., Marchis, F., & Ďurech, J. 2013, Icarus, 226, 1045
Hanuš, J., Marchis, F., Viikinkoski, M., Yang, B., & Kaasalainen, M. 2017, A&A, 599, A36
Levison, H. F., & Duncan, M. J. 1994, Icarus, 108, 18
Marchis, F., Descamps, P., Berthier, J., et al. 2008, Icarus, 195, 295
Nelder, J. A., & Mead, R. 1965, Comput, J, 7, 308
Nesvorný, D., Brož, M., & Carruba, V. 2015, in Asteroids IV, 297
Park, R. S., Folkner, W. M., Williams, J. G., & Boggs, D. H. 2021, AJ, 161, 105
Rivkin, A. S., Thomas, C. A., Howell, E. S., & Emery, J. P. 2015, AJ, 150, 198
Robert, C., & Casella, G. 2011, Handbook of Markov Chain Monte Carlo, 49
Schmid, H. M., Bazzon, A., Roelfsema, R., et al. 2018, A&A, 619, A9
Si, H. 2006, TetGen, `http://wias-berlin.de/software/tetgen/`
Tierney, L. 1994, Ann. Stat., 22, 1701
Torppa, J., Hentunen, V.-P., Pääkkönen, P., Kehusmaa, P., & Muinonen, K. 2008, Icarus, 198, 91
Vernazza, P., Marsset, M., Beck, P., et al. 2016, AJ, 152, 54
Vernazza, P., Ferrais, M., Jorda, L., et al. 2021, A&A, 654, A56
Viikinkoski, M., Kaasalainen, M., & Ďurech, J. 2015, A&A, 576, A8
Vilas, F., & Gaffey, M. J. 1989, Science, 246, 790
Yang, B., Wahhaj, Z., Beauvalet, L., et al. 2016, ApJ, 820, L35

Appendix A: MCMC figures

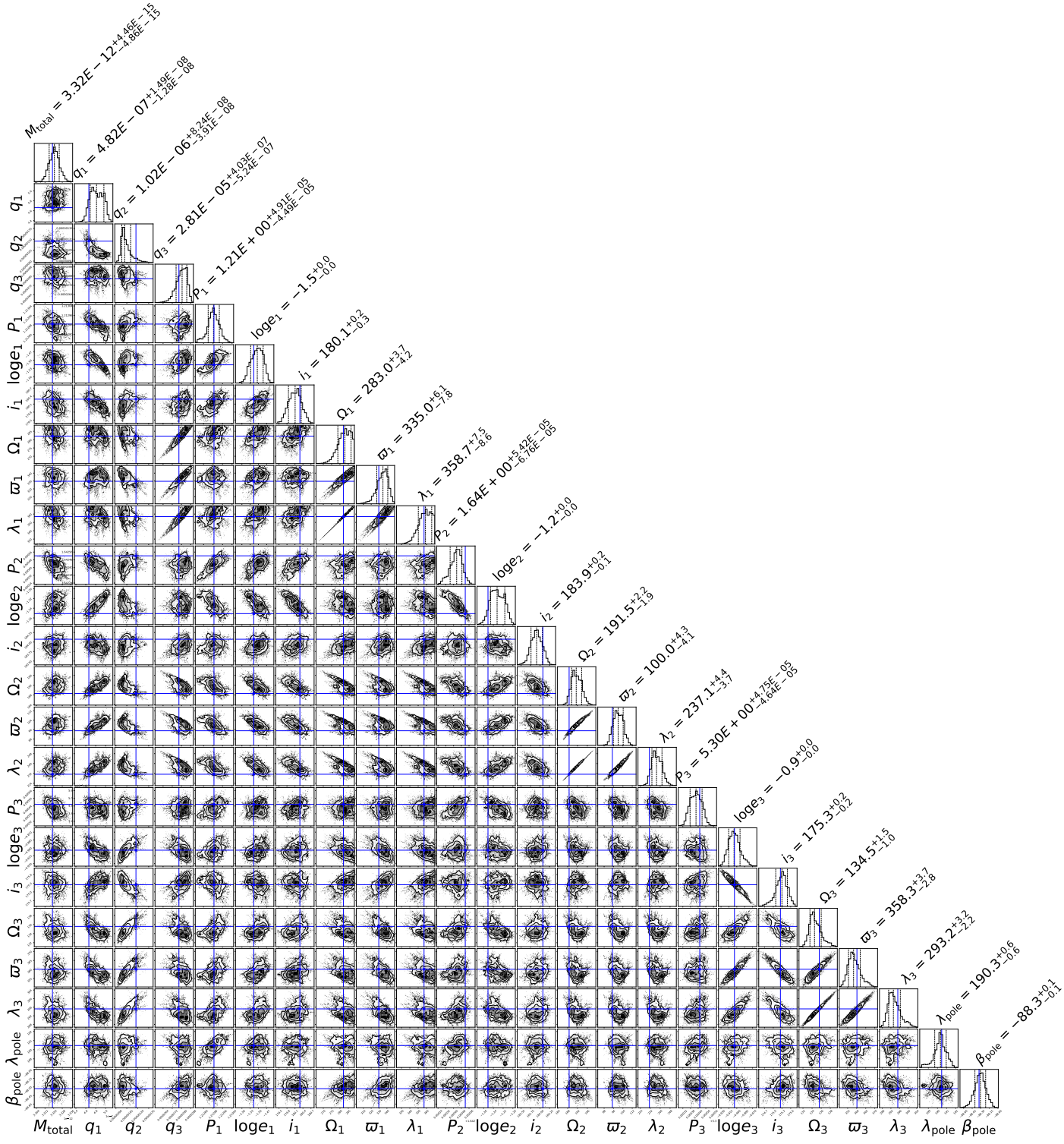

Fig. A.1. Corner plot showing the probability distributions of all parameters of the orbital model. *Blue* lines indicate a best-fit parameter, while the three *dashed* lines show the 16%, 50%, and 84% percentiles for each parameter.

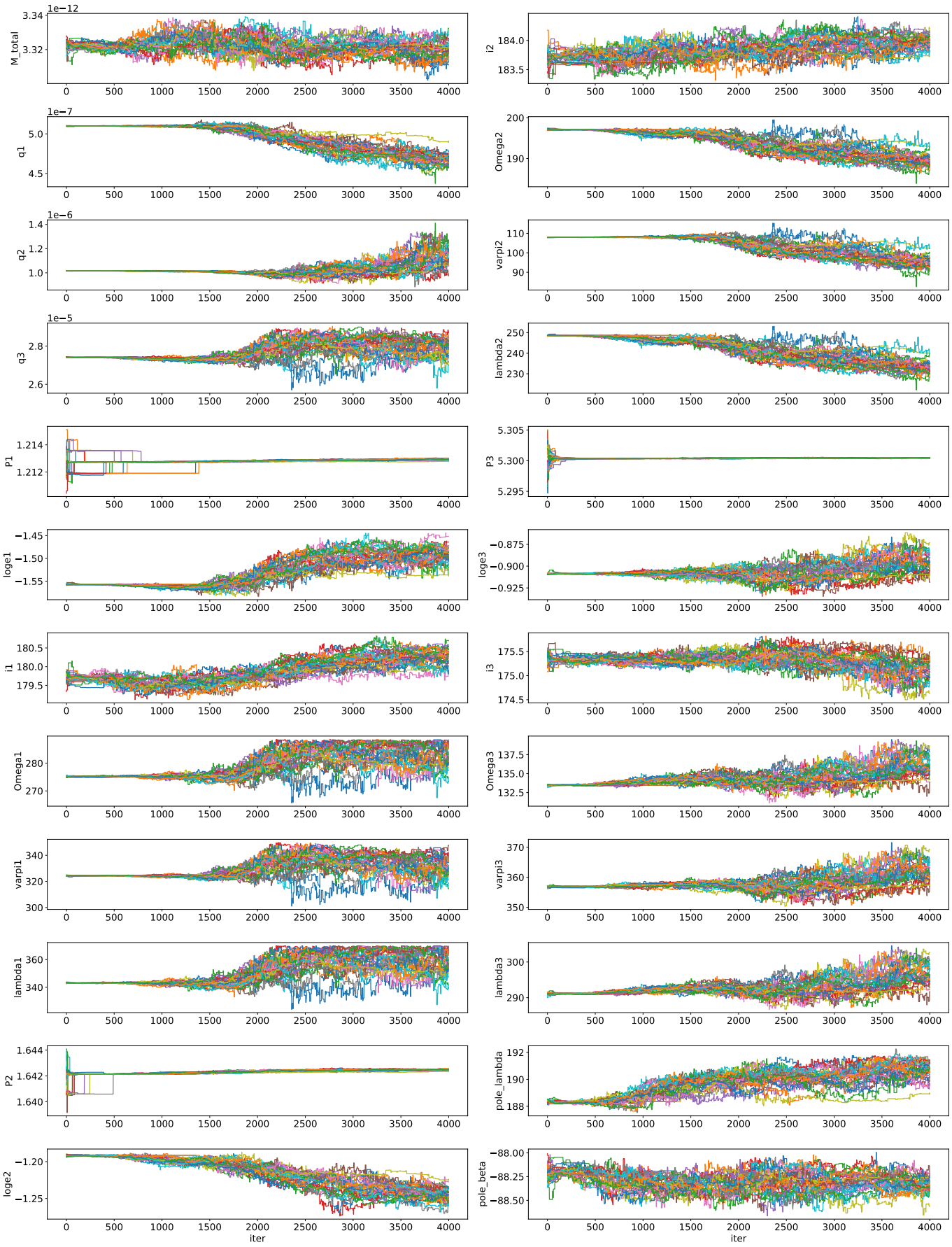

Fig. A.2. Markov chains. Each subplot corresponds to one variable and contains 33 walkers, each denoted by a different colour. Walkers, over 4000 iterations, mapped out possible values of the variables.

Appendix B: Observation data

In this Appendix, we present three tables of astrophotometry fits of the three moons of Elektra. In each table, x and y are the Cartesian positions of the moons relative to the photocentre of Elektra.

Table B.1. Astrophotometry fit of the inner moon S/2014 (130) 1.

July 2019 (Julian date)	x (mas)	y (mas)
2458694.861418	172.9	36.8
2458694.864054	177	37.5
2458694.866710	180	43.6
2458694.875133	188.7	46.5
2458694.877797	192.8	46.4
2458694.880464	196.2	47.4
2458694.883109	200.8	48.2
2458694.885767	207	49.7
August 2019 (Julian date)	x (mas)	y (mas)
2458699.760132	344.8	96.2
2458699.762773	346.2	99.7
2458699.765448	345.7	101.1
2458699.768099	349.2	105.4
2458699.770757	345.2	103.2
2458700.887314	275	83.1
2458700.897933	295.2	87
2458701.728692	-351.6	-120.7
2458701.731355	-341.9	-114.9
2458701.734024	-339.6	-115.9
2458701.736668	-348.2	-121.6
2458701.739317	-337.1	-118

Table B.2. Astrophotometry fit of the middle moon S/2014 (130) 2.

July 2019 (Julian date)	x (mas)	y (mas)
2458694.856099	366.6	169.1
2458694.858750	371.2	161.5
2458694.861418	377.6	160.5
2458694.864054	370.1	153.6
2458694.866710	362.1	153.6
2458694.875133	352.9	148.3
2458694.877797	353.1	148.8
2458694.880464	348.5	145.1
2458694.883109	349.4	153.9
2458694.885767	342.4	146.6
August 2019 (Julian date)	x (mas)	y (mas)
2458699.760132	340.2	154.7
2458699.762773	341.4	149.8
2458699.765448	340.2	153.2
2458699.768099	331.5	152.3
2458699.770757	321.3	148.2
2458701.728692	-228	-79.3
2458701.731355	-231.2	-83.3
2458701.734024	-233	-90.9
2458701.736668	-246.6	-88.6
2458701.739317	-247.7	-91.7

Table B.3. Astrophotometry fit of the outer moon S/2003 (130) 1.

July 2019 (Julian date)	x (mas)	y (mas)
2458694.85737	-663.6	-233.7
2458694.86799	-654	-233.9
2458694.87641	-651	-230
2458694.88704	-645.3	-227
August 2019 (Julian date)	x (mas)	y (mas)
2458699.69701	-915.2	-385.7
2458699.70762	-918.9	-388.3
2458699.76141	-898.5	-382.2
2458699.77203	-898.1	-379.5
2458700.88859	162.5	137.4
2458700.89921	188.4	147.5
2458701.72997	956.5	443.4
2458701.74059	960.9	445.7

Appendix C: Extension of the best-fit orbital model

In this section, we present an extension of the best-fit orbital model from Sect. 4. There are several astrometric measurements of the outer moon S/2003, from 2003 to 2006, which were published in Marchis et al. (2008). To further test our best-fit model, we extended it by about 10 years into the past and added these older measurements. With some additional converging, the resulting model has a $\chi^2 = 1406$. In Fig. C.1, we present the fit of the outer moon's orbit to the older positions.

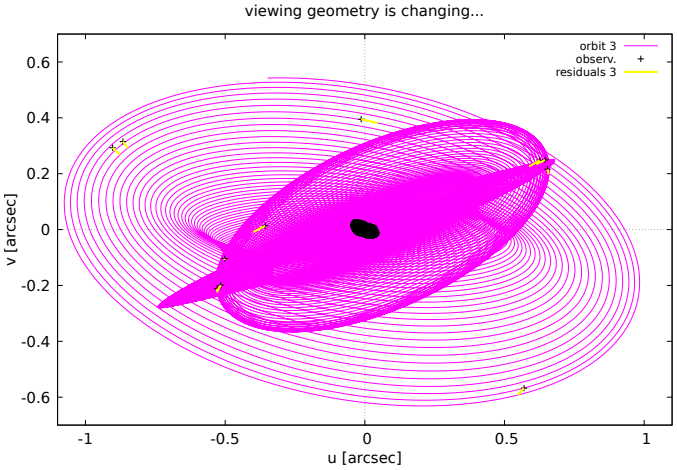

Fig. C.1. Extension of the best-fit quadrupole model, now with $\chi^2 = 1406$. Shown is only the relevant time span of 903 days for orbit 3. The orbit is plotted in the (u; v) coordinates (*pink* line), together with observed positions (*black crosses*), and residuals (*yellow* lines). The shape of Elektra for one of the epochs is overplotted in *black*.

Appendix D: Lightcurves

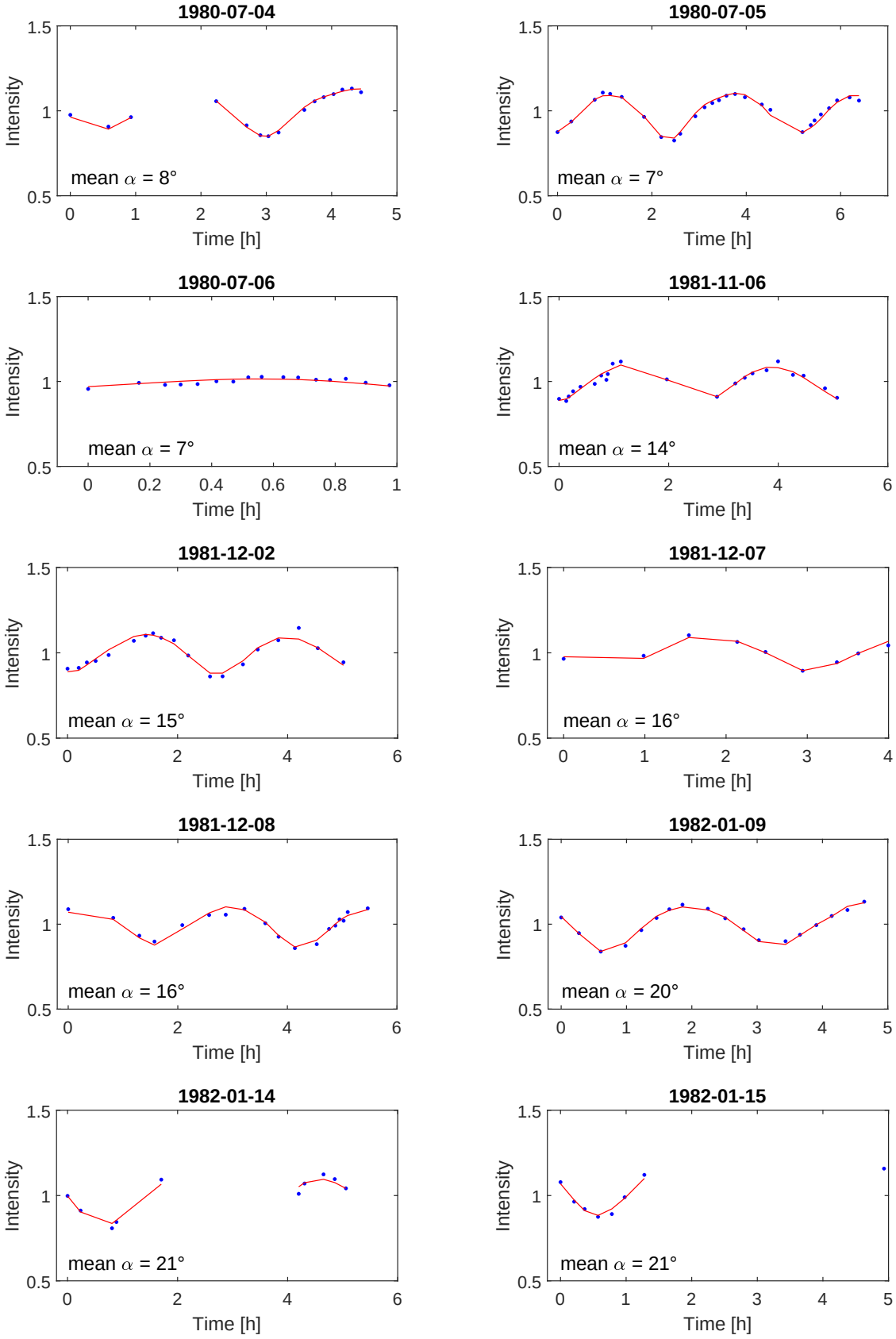

Fig. D.1. The light curves used in the shape reconstruction compared to the simulated light curves of the best-fit model. The observed intensity is represented by *blue dots*, while the simulated intensity of the shape model is depicted in *red*. The mean phase angle α for each observation is provided in the bottom left corner of each graph.

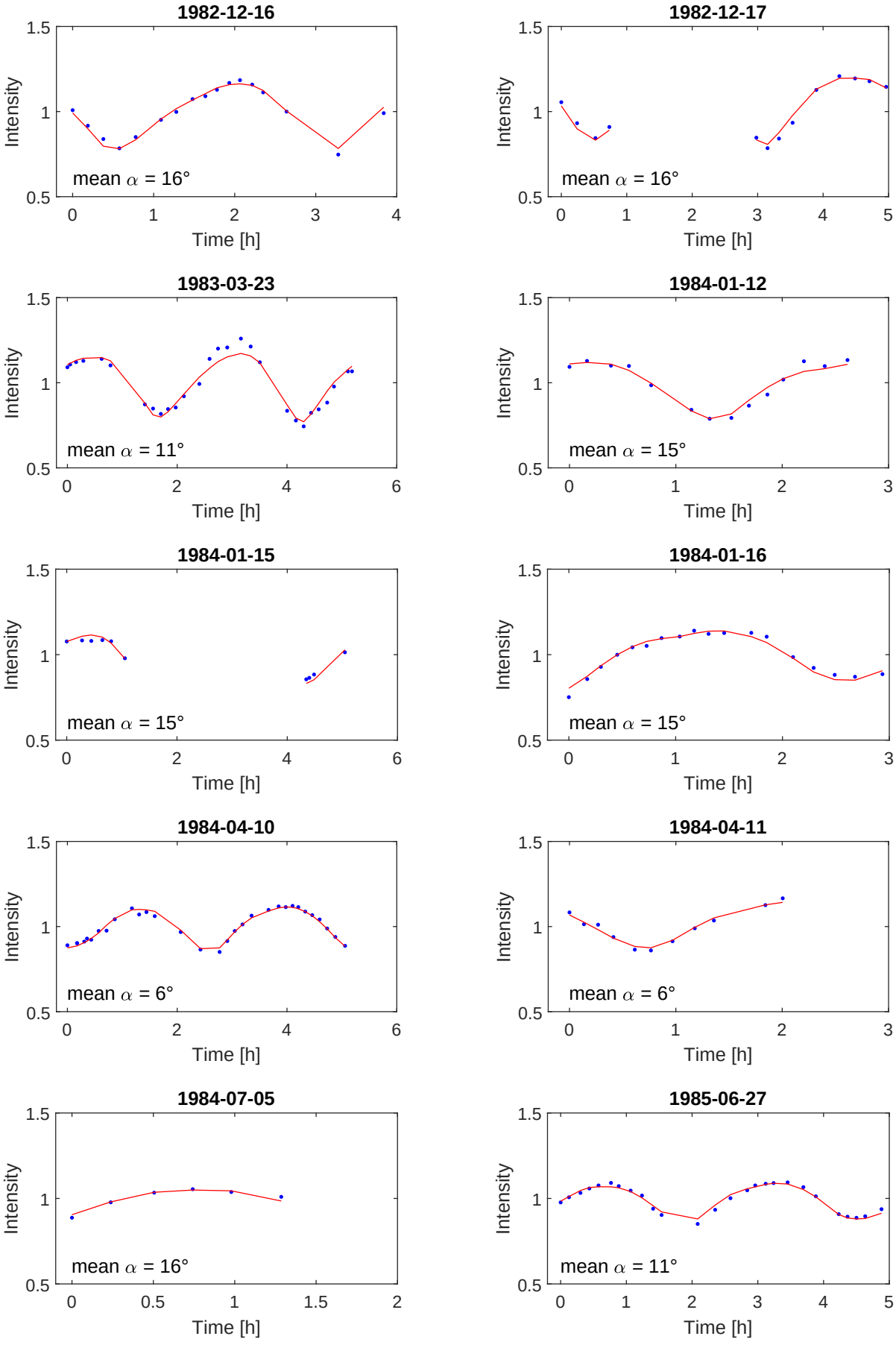

Fig. D.1. Continued.

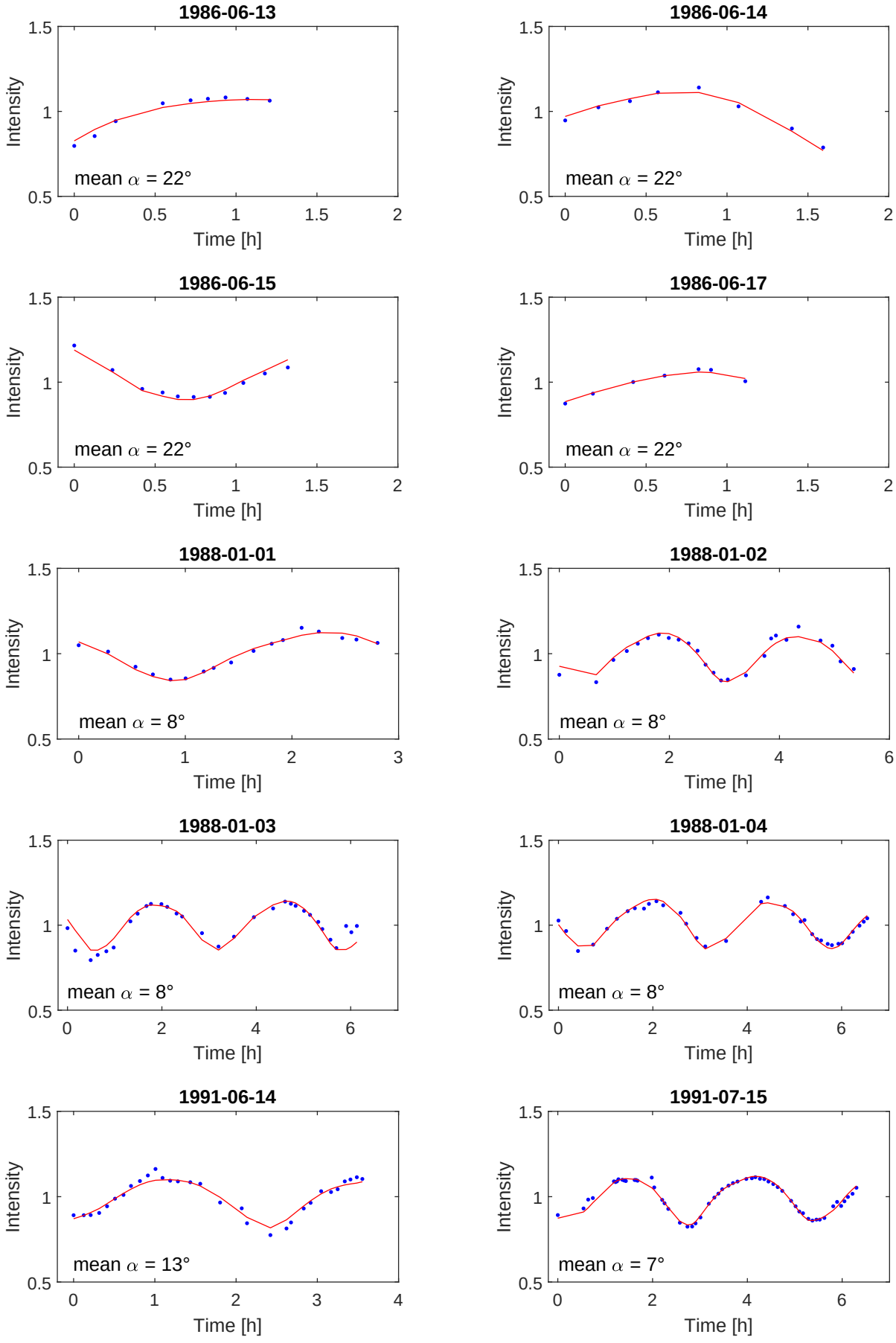

Fig. D.1. Continued.

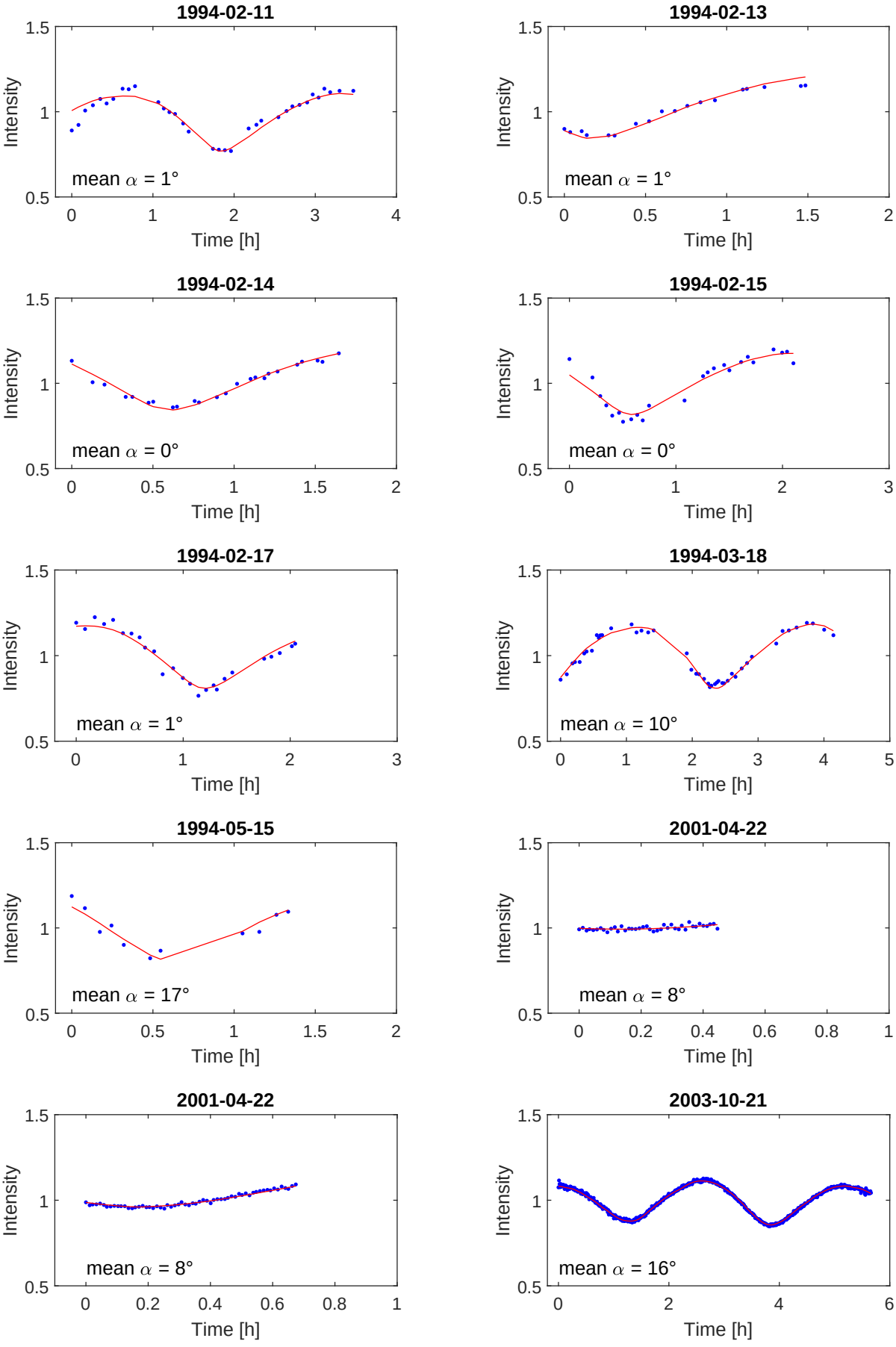

Fig. D.1. Continued.

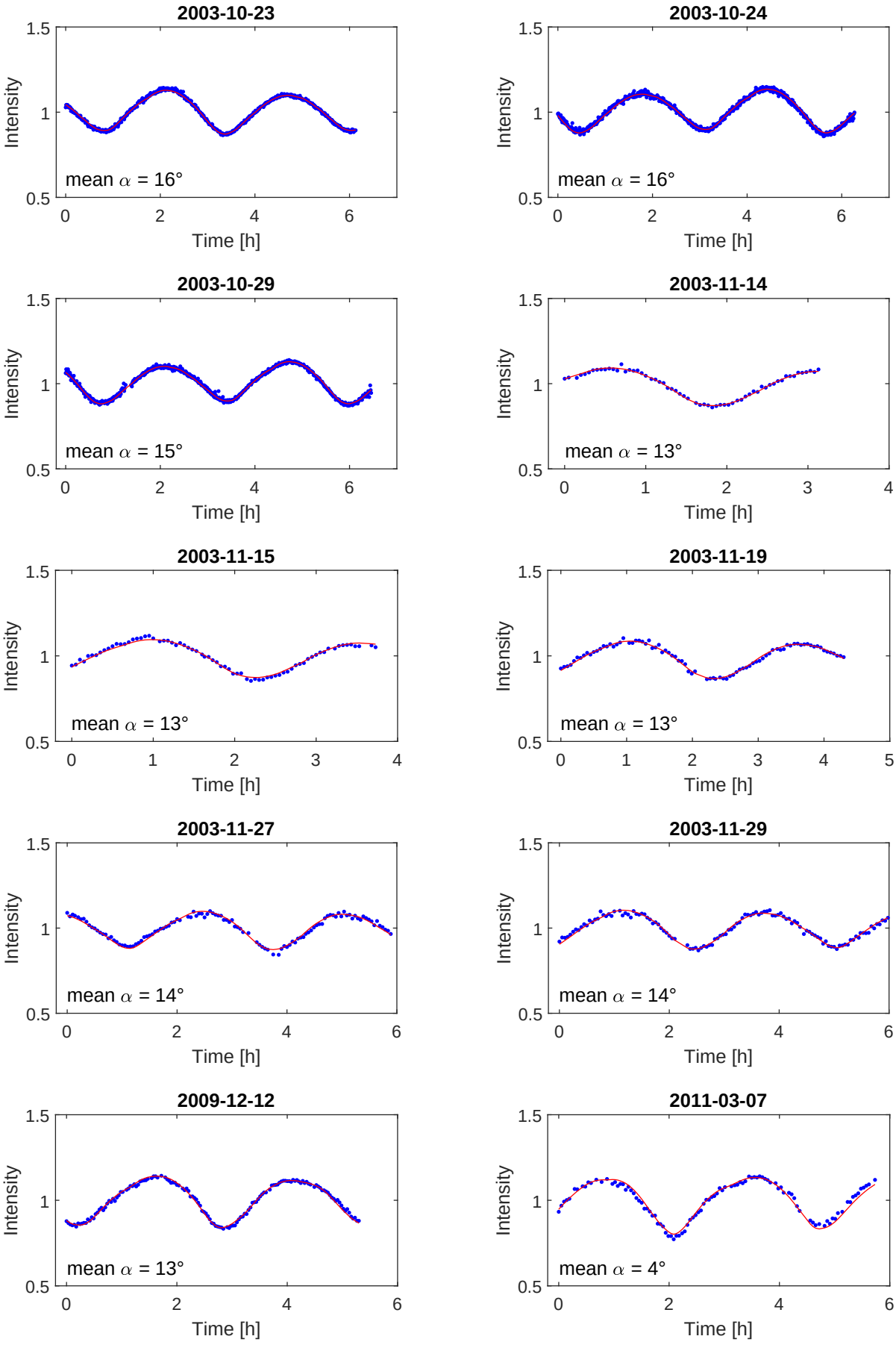

Fig. D.1. Continued.

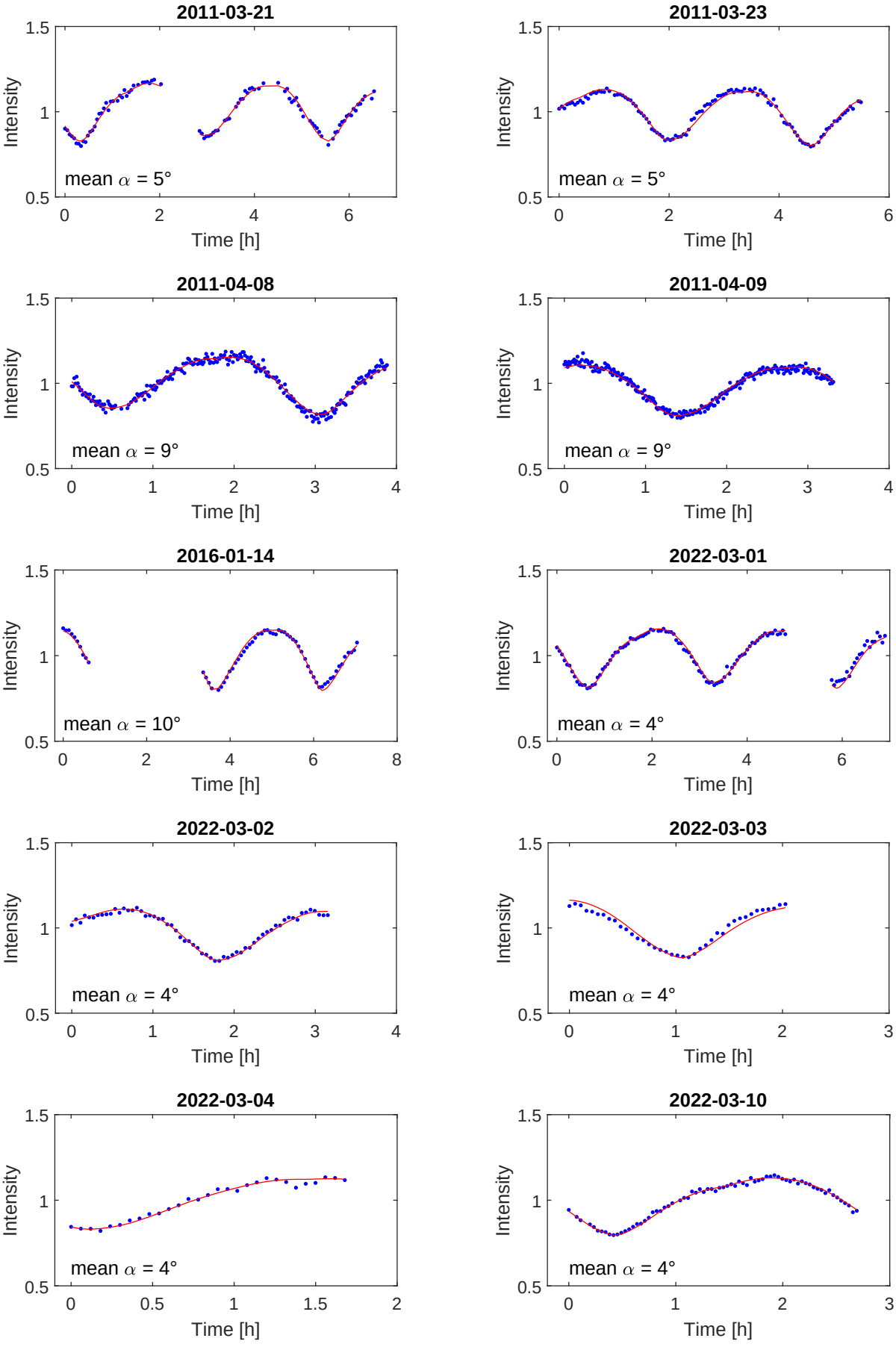

Fig. D.1. Continued.